1-1-2001

Dynamics of stars and globular clusters in M87

Aaron J. Romanowsky
San Jose State University, aaron.romanowsky@sjsu.edu

C. S. Kochanek
Harvard-Smithsonian Center for Astrophysics

Recommended Citation

DYNAMICS OF STARS AND GLOBULAR CLUSTERS IN M87

AARON J. ROMANOWSKY[1,2] AND CHRISTOPHER S. KOCHANEK[2]

ABSTRACT

We examine the dynamics of the stars and globular clusters in the nearby giant elliptical galaxy M87 and constrain the mass distribution, using all the available data over a large range of radii, including higher order moments of the stellar line-of-sight velocity distributions and the discrete velocities of over 200 globular clusters. We introduce an extension of spherical orbit modeling methods that makes full use of all the information in the data and provides very robust constraints on the mass models. We conclusively rule out a constant mass-to-light ratio model and infer that the radial density profile of the galaxy's dark halo falls off more slowly than r^{-2}, suggesting that the potential of the Virgo Cluster is already dominant at $r \sim 300'' \sim 20$ kpc.

Subject headings: galaxies: elliptical and lenticular, cD — galaxies: halos — galaxies: individual (M87) — galaxies: kinematics and dynamics — galaxies: star clusters — galaxies: structure — globular clusters: general

1. INTRODUCTION

Elliptical galaxies lack the dynamic simplicity of spiral galaxies, posing well-known challenges for determining their intrinsic properties (e.g., mass distribution, shape, orbit structure). The projected stellar velocity dispersion radial profile, $\hat{\sigma}_p(R)$, is easily measured but is subject to a degeneracy between the mass distribution and the orbital anisotropy, where radial variations in the stellar orbit types mask or mimic changes in the mass-to-light ratio (M/L) (Binney & Mamon 1982; Tonry 1983). Crucial for resolving this degeneracy is the measurement of higher order moments of the stellar line-of-sight velocity distributions (LOSVDs). Such LOSVD information has been used to constrain the masses of central supermassive black holes (van der Marel et al. 1998; Emsellem, Dejonghe, & Bacon 1999; Cretton & van den Bosch 1999; Gebhardt et al. 2000) and dark halos (Carollo et al. 1995; Rix et al. 1997; Gerhard et al. 1998; Saglia et al. 2000; Kronawitter et al. 2000). Unfortunately, the surface brightness of an elliptical galaxy declines rapidly with radius, making these measurements increasingly difficult at the large radii where the dark matter problem becomes most interesting ($\gtrsim 2$ effective radii [$R_{\rm eff}$]). Other techniques are necessary to probe this outer mass distribution.

In nearby galaxies, the two main candidates for such probes are X-ray emission from extended hot gas (see § 4.4 in Fabbiano 1989 for a review) and the discrete velocities of either planetary nebulae (see, e.g., Ciardullo, Jacoby, & Dejonghe 1993; Tremblay, Merritt, & Williams 1995; Hui et al. 1995; Arnaboldi et al. 1998) or globular clusters (see, e.g., Cohen & Ryzhov 1997, hereafter CR; Kissler-Patig et al. 1999; Zepf et al. 2000). However, the analysis of discrete kinematic measurements calls for more refined dynamic models than either simple virial estimators (see, e.g., Heisler, Tremaine, & Bahcall 1985; Kent 1990; Haller & Melia 1996) or binning the data and using the Jeans equations (see, e.g., Federici et al. 1993; Grillmair et al. 1994; Gebhardt & Fischer 1995; Tremblay et al. 1995). These pro-

cedures do not guarantee a physical solution, do make unwarranted assumptions about the orbital anisotropy, and do not make full use of the constraints provided by the data. The first two deficiencies are alleviated by techniques employing distribution function (DF) basis sets that permit the full freedom of orbit types (see, e.g., Merritt, Meylan, & Mayor 1997; Mathieu & Dejonghe 1999; Saglia et al. 2000). But these techniques typically bin the data in radius and velocity, destroying potentially useful information, such as the maximum observed velocity as a direct constraint on the escape velocity. More general methods are needed to make better use of the information contained in the discrete velocity data; Merritt & Saha (1993) and Merritt (1993) have demonstrated one such approach using DF basis sets and maximum likelihood methods. We develop a general dynamic method based on orbit modeling and apply it to a real galaxy, M87.

The giant central Virgo Cluster galaxy M87 (=NGC 4486), although not a typical elliptical galaxy, is nevertheless a prime candidate for modeling because of the abundance of data available on it. In addition to high-precision measurements of its higher order stellar velocity moments and the radially extended velocity dispersion, it has the largest available sample of globular cluster (GC) velocity measurements. The stellar velocity measurements extend out to $\sim 1.5R_{\rm eff}$ and the GC measurements to $\sim 5R_{\rm eff}$, probing well into the area where the dynamics are presumably dominated by the dark halo of the galaxy or of the Virgo Cluster. The combination of these kinematic constraints should provide robust limits on the dark matter distribution and on the orbital structures of both the stars and the GCs.

While a variety of modeling techniques have been used to study the stellar dynamics of M87 (Sargent et al. 1978; Duncan & Wheeler 1980; Binney & Mamon 1982; Newton & Binney 1984; Richstone & Tremaine 1985; Dressler & Richstone 1990; Tenjes, Einasto, & Haud 1991; van der Marel 1994; Merritt & Oh 1997), they all concentrated on its central regions in order to constrain the mass of a central black hole. The stellar dynamics of its *halo* have not been modeled in detail nor have the higher order velocity moments been used as strict constraints, but the best available tracers of the halo mass distribution are ultimately the

[1] Kapteyn Astronomical Institute, Postbus 800, 9700 AV Groningen, Netherlands; romanow@astro.rug.nl.

[2] Harvard-Smithsonian Center for Astrophysics, MS-51, 60 Garden Street, Cambridge, MA 02138; ckochanek@cfa.harvard.edu.

GCs and the hot gas, which can be easily observed at large radii. Some simple dynamic methods have been used to estimate the halo mass using the GCs (Merritt & Tremblay 1993; CR). They claim that the radially rising velocity dispersion profile rules out a constant M/L model and that it suggests that the GCs are in fact tracing the Virgo Cluster potential rather than M87's own potential (as suggested also by analyses of the X-ray emission and the kinematics of the cluster galaxies; e.g., see Nulsen & Böhringer 1995; McLaughlin 1999). However, a more rigorous dynamic model, allowing for the systematic orbital uncertainties, is necessary to confirm these findings. We will apply our general orbit modeling method, using a large sample (~ 200) of discrete GC velocities, to see how the GCs—alone and jointly with the stellar dynamics—constrain the mass distribution. In § 2 we detail the observational constraints for M87. In § 3 we describe our modeling methods. In § 4 we present the results, and the conclusions are in § 5.

2. OBSERVATIONAL CONSTRAINTS

Here we summarize the observational constraints on M87. These include the stellar surface brightness (§ 2.1), the velocity measurements of the stars (§ 2.2), the globular cluster surface density (§ 2.3), and the globular cluster discrete velocity measurements (§ 2.4). We assume a distance to M87 of 15 Mpc (Pierce et al. 1994), so that $1'' = 73$ pc and $1' = 4.4$ kpc. The stellar effective radius is $R_{eff} \simeq 100''$ (Burstein et al. 1987; Zeilinger, Møller, & Stiavelli 1993).

2.1. Stellar Surface Brightness

For the stellar surface brightness radial profile $\mu(R)$ in the core region ($R = 0''.01–8''$), we use the *Hubble Space Telescope I*-band data of Lauer et al. (1992). We use their seeing-deconvolved profile and approximate the photometric uncertainties by $\Delta\mu = \max [0''.011/R, 0.02]$. For the outer regions ($R = 8''–745''$), we use the *B*-band data of Caon, Capaccioli, & Rampazzo (1990), with the photometric uncertainties estimated from their Figure 3 and with an offset of 2.78 mag to match the profile to the Lauer et al. (1992) data. The color gradients are quite small over the entire range of the galaxy [$|\Delta(B−I)|_{max} < 0.2$ mag; e.g., Boroson, Thompson, & Shectman 1983; Cohen 1986; Zeilinger et al. 1993], so there should be little systematic problem in combining the *I*-band and *B*-band data. The isophote ellipticity varies from 0.02 at $2''$ to 0.1 at $75''$ to 0.35 at $500''$. The dynamics of the galaxy depend on the ellipticity of its gravitational potential, which is much rounder than its density distribution ($\epsilon_\Phi \sim \epsilon_\rho/3$; § 2.3.1 in Binney & Tremaine 1987), so it will be a reasonable approximation to treat the galaxy as spherical. We map all of the data from the major axis a to the intermediate axis $m = a(1 − \epsilon)^{1/2}$.

For the purposes of our mass modeling, we project and fit a parameterized luminosity density model to the data of the form $v_*(r) = v_0(r/s_1)^{-\alpha_1}(1 + r^3/s_2^3)^{-\alpha_2}(1 + r/s_3)^{-\alpha_3}$ and find $v_0 = 9.9 \times 10^6 L_{B,\odot}$ arcsec^{-3}, $\alpha_1 = 1.22$, $\alpha_2 = 0.361$, $\alpha_3 = 1.26$, $s_1 = 1''$, $s_2 = 9''.38$, and $s_3 = 170''$, with a χ^2 statistic for the fit of 35.1 for 142 degrees of freedom. This functional fit will only be used to generate a constant M/L gravitational potential, while we will directly fit the surface brightness data in our dynamic models (§ 3). Note that in M87, $\mu(R)$ does not taper off steeply in the outer regions as in normal $R^{1/4}$ elliptical galaxies—a typical R^{-2} cD envelope (Schombert 1986) begins at $R \gtrsim 300''$. An old dispute over

the brightness of this envelope (see, e.g., de Vaucouleurs & Nieto 1978; Carter & Dixon 1978) has not been resolved, presumably because of sky-subtraction problems for such a large, low surface brightness structure. Our asymptotic radial slope lies between the reported extremes.

2.2. Stellar Velocities

For the core region ($R < 29''$), we use the *G*-band data from van der Marel (1994, hereafter vdM) for the projected stellar velocity dispersion $\hat{\sigma}_p(R)$ and the Gauss-Hermite velocity moments $h_4(R)$ and $h_6(R)$ (see § 3). For the outer regions ($R = 28''–168''$), we use $\hat{\sigma}_p(R)$ from Sembach & Tonry (1996, hereafter ST). We combine the data from positive and negative radii into one radial profile. There appears to be a systematic velocity offset between the ST data and most other data (Sargent et al. 1978; Davies & Birkinshaw 1988; Jarvis & Peletier 1991; Winsall & Freeman 1993), presumably due to the large slit width; we estimate that this corresponds to an additional instrumental dispersion of 183 ± 11 km s^{-1}, which we remove from the ST data in order to match them to the vdM data. The final velocity dispersion profile is nearly constant for $R < 1''$, outside of which it falls off slowly with radius ($\hat{\sigma}_p \sim R^{-0.1}$). Comparing h_4 and h_6 from positive and negative radii, we find differences larger than are consistent with the stated uncertainties. We assume that the errors were underestimated by 12% and 22%, respectively, to bring the profiles into statistical agreement. The departures from Gaussianity of the LOSVD are everywhere small (typically, $|h_4|, |h_6| < 0.02$).

2.3. Globular Cluster Surface Density

Our GC surface density radial profile $N(R)$ is taken from the number counts of Kundu et al. (1999) for $R = 0''–96''$ (with their quoted uncertainties). For $R = 84''–472''$, we take the data from McLaughlin, Harris, & Hanes (1993), adding in their 0.4 arcmin^{-2} background uncertainty and multiplying by 1.45 to match the normalization of the Kundu et al. (1999) data. For $R = 419''–1351''$, we use the data from Harris (1986) after subtracting their background count of 5.8 ± 0.3 arcmin^{-2} and normalizing by a factor of 2.19. We do not convert any of these profiles to an intermediate axis since this is already effectively accomplished by the derivation method (counting in circular annuli). Like the stellar surface brightness, the GC surface density decreases slowly with radius in the central regions ($\sim R^{-0.3}$) and changes over to a steeper power law in the outer parts ($\sim R^{-1.6}$); however, the radius where this break occurs is much larger for the GCs ($\sim 60''$ vs. $\sim 10''$), demonstrating that these systems are dynamically distinct.

2.4. Globular Cluster Discrete Velocities

For the GC line-of-sight velocities v_z, we use data from Mould, Oke, & Nemec (1987), Huchra & Brodie (1987), Mould et al. (1990), CR, and Cohen (2000). Most of the positions are taken from Strom et al. (1981). We compare the velocities of common objects to determine the systematic offset between the data sets and to estimate the measurement uncertainties ($\Delta v_z \sim 100$ km s^{-1}). We discard as foreground stars all objects with heliocentric velocities $v_z < 250$ km s^{-1} and as background galaxies all those with $v_z > 2650$ km s^{-1}. We examine the colors and magnitudes of objects with $v_z < 500$ km s^{-1} to distinguish GCs from stars. Objects of uncertain identification are discarded. We map the data to the intermediate axis m, using ellipticity esti-
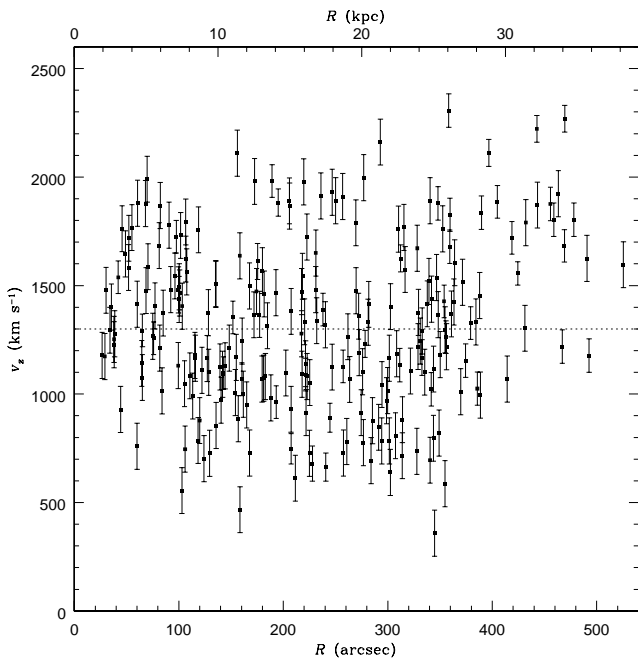
FIG. 1.—Line-of-sight velocities for 234 GC around M87 as a function of galactocentric radius R. The dotted line shows a systemic velocity of 1300 km s^{-1}.

mates from McLaughlin, Harris, & Hanes (1994). Our final data set has 234 velocities from $R = 25''-526''$ (see Fig. 1).

There is a paucity of low-velocity measurements at large radii, which may be related to the rotation of the GCs along the galaxy's major axis in the outer parts, as demonstrated by Kissler-Patig & Gebhardt (1998). For the GCs with $R \geq 370''$, there were only four measurements taken on the "approaching" side and 23 on the "receding" side. Thus,
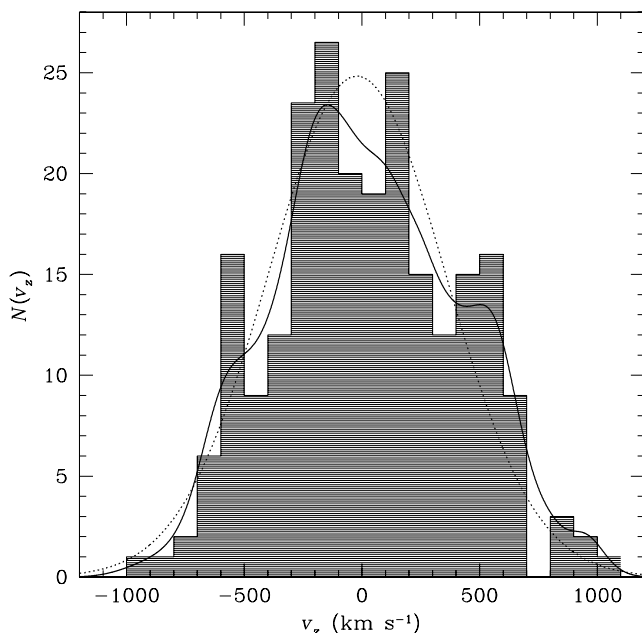

FIG. 2.—Distribution of globular cluster line-of-sight velocities relative to a systemic velocity of 1300 km s^{-1}. The histogram shows the number of data points in velocity bins. The solid curve shows a smoothed superposition of the measurements. The dotted curve shows the best-fit Gaussian curve to the data ($\sigma = 376$ km s^{-1}). Note the double peaks of low significance at ± 200 and at ± 500 km s^{-1}.

the large-radius velocity asymmetry is probably due to incomplete spatial coverage, which may make our mean velocity for the system systematically high (it is decreased from 1352 to 1293 km s^{-1} if the clusters with $R \geq 370''$ are omitted). This is also suggested by the global velocity distribution (Fig. 2), which appears more symmetric if the mean velocity is set to ~ 1300 km s^{-1}. The best-fit Gaussian curve to the data has a central velocity of $\hat{v}_p = 1323 \pm 28$ km s^{-1} (1308 $\pm$ 29 km s^{-1} if the outer clusters are omitted). We adopt a systemic velocity of 1300 km s^{-1}, which we subtract from the measurements to get the galactocentric velocities. This compares well with estimates of the stellar mean redshift from vdM (1277 km s^{-1}), ST (1293 km s^{-1}), and the Third Reference Catalogue of Bright Galaxies (1282 $\pm$ 9 km s^{-1}; de Vaucouleurs et al. 1991). The large-radius velocity asymmetry will not pose any further difficulties because we will model only the *even* part of the DF so that all the discrete velocities are implicitly considered as present also at their reflected position about the mean velocity.

Figure 2 also suggests that the GCs have a tangentially biased orbit distribution, which typically produces a flat or double-peaked LOSVD. We fit a fourth-order Gauss-Hermite velocity moment (see § 3) to the system, finding $h_4 = -0.04 \pm 0.02$ ($\hat{\sigma}_p = 404 \pm 16$ km s^{-1}), which is weakly suggestive of tangential anisotropy. A double-peaked LOSVD (especially evident at larger radii) has also been found in the GC system of the Fornax Cluster cD galaxy NGC 1399 (Kissler-Patig et al. 1999).

3. METHODS

The method of orbit modeling was pioneered by Schwarzschild (1979) to reproduce the observed density distribution of a galaxy from a weighted library of representative particle orbits. Given a fixed gravitational potential $\Phi(r)$, the solutions are nonparametric—no functional form is assumed for the DF—so that one need not worry that the models cannot fully explore the possible solutions. The DF is guaranteed to be nonnegative and physical. This method was extended by Richstone & Tremaine (1984) to include projected velocity dispersion information and by Rix et al. (1997) to include higher order velocity moments. We used similar techniques to examine the uncertainty in a high-redshift galaxy's mass as implied by a measurement of its central velocity dispersion—an important step in determining H_0 from certain gravitational lens systems (Romanowsky & Kochanek 1999, hereafter Paper I). Other recent orbit modeling efforts have concentrated on applying the method to three-integral axisymmetric systems (e.g., van der Marel et al. 1998; Cretton & van den Bosch 1999; Gebhardt et al. 2000; Cretton, Rix, & de Zeeuw 2000). Here we extend our spherical method to include the discrete velocities of GCs. The outline of the method is as follows:

We begin with an assumed radial profile for the mass density distribution $\rho(r)$. Our first model is a simple representation of a dark matter–dominated system, the singular isothermal sphere (SIS): $\rho(r) = \sigma_0^2/2\pi G r^2$. The second model is the constant M/L distribution described in § 2.1, parameterized by Υ_B: the ratio of the mass density $\rho(r)$ and the B-band luminosity density $v_*(r)$, with units of $M_\odot/L_{\odot, B}$. We pick a random distribution of orbits that densely samples the phase space of energy and angular momentum $(E, |L|)$. The initial radii r_{0k} of the orbits are logarithmically

spaced in r_0, and the energy E_k of each orbit is selected to correspond to that of a circular orbit at this radius, $\Phi(r_{0k}) + v_c^2(r_{0k})/2$. For the SIS model, this procedure produces a sampling that is uniform in energy. The angular momentum L_k of the orbit is selected randomly from the range $[0, L_{\max, k}]$, where $L_{\max, k} = r_{0k} v_c(r_{0k})$. For both the stellar and GC models, we use 2500 particle orbits. For the stars, r_0 spans the range $0\rlap{.}{''}07$–$4450''$, resulting in a radial coverage of $r = 0''$–$7330''$ (SIS model) or $r = 0''$–$8710''$ (constant M/L model). For the GCs, $r_0 = 10\rlap{.}{''}0$–$13,360''$, corresponding to $r = 0''$–$22,030''$ (SIS model) or $r = 0''$–$26,420''$ (constant M/L model).

We next compute the orbit projection "kernels," which correspond to the contribution of each orbit to each observable. The predictions of the model can then be expressed as follows:

$$y_i^m = \sum_k w_k^2 \langle K_{ik} \rangle_{t, \theta, \phi} , \qquad (1)$$

where the w are the orbit weights, and the kernels $\mathbf{K}$ have been averaged over time and all spherical-polar viewing angles (θ, ϕ). For example, the kernel for the angle-averaged surface density in an annulus between R_1 and R_2 of an orbit at an instantaneous radius r' is given by the integral

$$\langle K_{I(R_1, R_2)} \rangle_{\theta, \phi}(r') = \frac{1}{\pi(R_2^2 - R_1^2)} \int_{R_1}^{R_2} 2\pi R \, dR$$
$$\times \int_R^\infty \frac{\delta(r - r')}{4\pi r^2} \frac{2r \, dr}{\sqrt{r^2 - R^2}} \int_0^{2\pi} \frac{d\xi}{2\pi} \quad (2)$$
$$= \frac{\sqrt{1 - R_1^2/r'^2} - \sqrt{1 - R_2^2/r'^2}}{\pi(R_2^2 - R_1^2)} , \qquad (3)$$

where the orbit's instantaneous density is $\delta(r - r')/4\pi r^2$, the variable ξ represents the line of sight's position in the tangential plane (θ, ϕ), and the integration is carried out along the line of sight $z = \pm(r^2 - R^2)^{1/2}$. The viewing angle integral (along $d\xi$) is nontrivial for kernels that involve velocity measurements. Placed at the initial radius r_0, the orbit is run forward in time for one radial period T_r, and the final kernel is found by averaging over time:

$$\langle K \rangle_{t, \theta, \phi} = \frac{1}{T_r} \int_0^{T_r} \langle K \rangle_{\theta, \phi}(t) \, dt ,$$

where the integration is handled by a Bulirsch-Stoer–type integrator.

We must calculate the model's LOSVD, $dL/dv_p(v_p, R)$, to fit the observed stellar velocity moments $(\hat{\sigma}_p, h_4, h_6)$ and the GC velocity measurements. The LOSVD kernels $K_{dL/dv_p(R), k}$ for a measurement at radius R are binned in velocity with $v_p = [0, \ldots, v_{\max}]$, where $v_{\max}(R)$ is the velocity of a particle at radius $r = R$ that has plunged inward on a radial orbit from the largest possible radius. For the constant M/L model, this implies that $v_{\max} \simeq v_{\rm esc}$ (the escape velocity). Our models are symmetric in velocity, i.e., $dL/dv_p(v_p) = dL/dv_p(-v_p)$. By construction, $v_{\max}^2$ scales linearly with the mass normalization of the galaxy model (σ_0^2 or Υ_B) so that we can use the same binned LOSVD kernels when changing the mass scale.

The Gauss-Hermite velocity moments h_l, which measure deviations of a LOSVD from a Gaussian, are defined by

$$h_l \equiv \frac{\sqrt{2}\gamma_0}{\hat{\gamma}_p} \int_{-\infty}^\infty \frac{dL}{dv_p}(v_p) e^{-\hat{w}^2/2} H_l(\hat{w}) \, dv_p , \quad (4)$$

where $\hat{w} = (v_p - \hat{v}_p)/\hat{\sigma}_p$, γ_0 is the line strength, $(\hat{\gamma}_p, \hat{v}_p, \hat{\sigma}_p)$ are the coefficients for the best Gaussian fit to dL/dv_p, and $H_l(\hat{w})$ are the Hermite polynomials (van der Marel & Franx 1993). The moments (h_4, h_6) measure how flat ($h_4 < 0$, $h_6 > 0$) or how peaked ($h_4 > 0$, $h_6 < 0$) the LOSVD is compared to a Gaussian, where these signatures are typically produced by tangential and radial orbits, respectively. The two moments differ in how much weight they put in the high-velocity wings of the LOSVD. In Paper I, we fitted a Gaussian curve to the LOSVD to find $(\hat{\gamma}, \hat{\sigma}_p)$ at each step in our minimization routine and then calculated h_4; this is equivalent to solving the nonlinear equations $h_0 = 1$ and $h_2 = 0$. Here, we expand the Gauss-Hermite series about the fixed data values $\hat{\sigma}_p^d$. Rather than directly fitting $\hat{\sigma}_p^d$, we equivalently fitted the second-order moment $h_2 = 0.00 \pm \Delta h_2$, where $\Delta h_2 \simeq \Delta\hat{\sigma}_p/\sqrt{2}\hat{\sigma}_p^d$. With this formulation, calculating the model's velocity observables is now linear with respect to the orbit weights. We use 41 velocity bins from $v_p = 0$ to $v_{\max}$ to numerically integrate equation (4), which we have heuristically found to give very good accuracy. Note that because our model is completely spherically symmetric (simulating only the even part of the DF), it would be more appropriate to fit measurements of z_4 (expanded around $\hat{v}_p = 0$) rather than h_4 (see § 5.1 in van der Marel et al. 1994); however, these measurements are not available for M87. Since the measured rotation is small (~ 10 km s^{-1}), the difference would be unimportant.

The kernels $(\mathbf{K}_I, \mathbf{K}_{dL/dv_p})$ need be computed only once for each galaxy mass model. We then adjust the weights of the orbits so that the model's projected observables y^m (eq. [1]) best fit the data y^d. For most of the data $(I, \hat{\sigma}_p, h_4, h_6)$, we express the likelihood of the fit using the standard χ^2 statistic,

$$\chi^2 = \sum_i \left(\frac{y_i^m - y_i^d}{\sigma_i} \right)^2 , \qquad (5)$$

where the measurement uncertainty is σ_i, while the likelihood function for the discrete velocities and positions of the GCs is

$$\mathcal{L}_i(v_i, R_i) \propto \int \frac{dL}{dv_p}(v_p, R_i) e^{-(v_i - v_p)^2/2\sigma_i^2} \, dv_p , \quad (6)$$

where $v_i \pm \sigma_i$ are the individual velocity measurements. In maximizing $\mathcal{L}_i$, we are forcing the LOSVD to peak at the measured velocities v_i weighted by the measurement errors σ_i. This is schematically illustrated in Figure 3. Given complete freedom, this method would produce a best-fit solution whose LOSVDs resembled δ-functions at the measurements v_i. However, the model's averaging in angle and time produces an intrinsic smoothing to the LOSVDs and does not permit such unphysical solutions. For the current implementation, we use 15 velocity bins from $v_p = 0$ to $v_{\max}$ for the LOSVD at each radius in order to compute the integral in equation (6). Note that our method does not require binning the velocities in radius nor computing velocity moments.

The final function that we will minimize is

$$f(w) \equiv \tfrac{1}{2}\chi^2 - \sum_i \ln \mathcal{L}_i + \lambda S , \qquad (7)$$

where S is a measure of entropy:

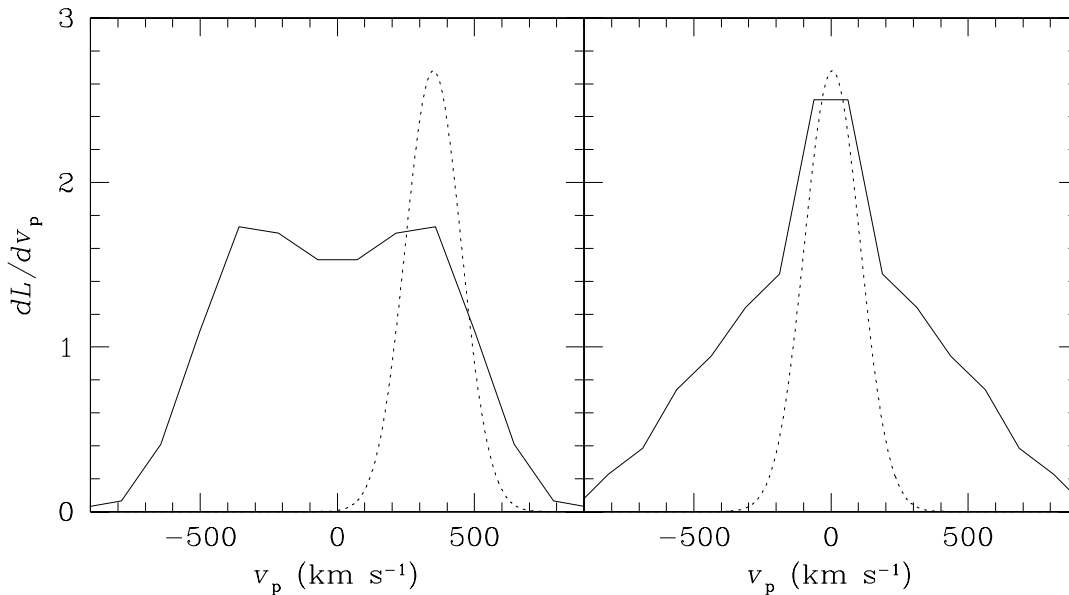$$S = \sum_k w_k^2 \ln w_k^2 . \qquad (8)$$

Fig. 3.—Schematic LOSVDs (*solid curves*) fitted to discrete velocity data (*dotted curves*). The double-peaked LOSVD on the left is indicative of tangential anisotropy, while the centrally peaked LOSVD on the right indicates radial anisotropy.

We employ this smoothing function S as a heuristic device for quickly reaching a rough solution; in our final solutions, the Lagrangian factor λ is reduced to such a low value ($\sim 10^{-5}$) so as to make the entropy constraints inconsequential. With no such regularization imposed, this is an ill-conditioned inversion problem, so our DF solutions will be choppy in a way that real galaxies' DFs presumably are not. However, our methods are the statistically correct way to handle the uncertainties, absent any other a priori smoothness conditions. We use a conjugate gradient method (see § 10.6 in Press et al. 1992), with first and second derivative information, to minimize f. We have tested our methods on an isotropic Hernquist (1990) model to demonstrate that we recover correctly the input mass, given constraints on $I(R)$ and $\hat{\sigma}_p(R)$ (see Paper I).

4. RESULTS

Here we present the results of our modeling. First we investigate the necessity for dark matter in the system by comparing two simple models (§ 4.1). Then we consider more generalized mass models (§ 4.2). Finally, we report constraints on the orbit anisotropies (§ 4.3).

4.1. Test for Dark Matter

We first fitted the two simple mass models (SIS and constant M/L) to the stellar data $[I(R), \hat{\sigma}_p(R), h_4(R), h_6(R)]$ over a sequence of the mass parameters σ_0 and Υ_B (see Fig. 4). Table 1 lists the best-fit values for these parameters and the difference in log likelihood between the two models. For the SIS model, we find $\sigma_0 = 272^{+19}_{-5}$ km s^{-1}; the fit of the best solution to the data is shown in Figure 5. For the constant M/L model, we find $\Upsilon_B = 8.1 \pm 0.6$. This model does not fit the data as well as the best SIS model does (1 σ significance), providing weak evidence for a dark matter halo in this galaxy.

In order to see which constraints are important for indicating the presence of dark matter, we have tried models that lack either the $h_6(R)$ data or the large-radius $\hat{\sigma}_p(R)$ data (Table 1). Dropping these constraints makes little difference in differentiating between mass models (though the mass normalization of the SIS model does change in the latter case). In particular, we note that the extra velocity dispersion data are unhelpful, owing to the flexibility of the orbital anisotropies to reproduce an arbitrary velocity dispersion profile. Only with additional LOSVD information at large

TABLE 1
SIMPLE M87 MODEL SOLUTIONS

| | SINGULAR ISOTHERMAL | CONSTANT M/L | |
| | σ_0 | Υ_B | |
CONSTRAINTS	(km s^{-1})	($M_\odot/L_{\odot, B}$)	$\Delta \ln \mathscr{L}$
Stars: I, $\hat{\sigma}_{vdM}$, $\hat{\sigma}_{ST}$, h_4, h_6	272^{+19}_{-5}	8.1 ± 0.6	0.8 ($1.0\ \sigma$)
Stars: I, $\hat{\sigma}_{vdM}$, $\hat{\sigma}_{ST}$, h_4	275^{+19}_{-9}	$8.1^{+0.7}_{-0.6}$	0.6 ($0.9\ \sigma$)
Stars: I, $\hat{\sigma}_{vdM}$, h_4, h_6	254^{+22}_{-18}	$8.3^{+1.0}_{-1.7}$	0.9 ($1.0\ \sigma$)
GCs	409^{+36}_{-24}	$42.9^{+3.3}_{-3.1}$	12.9 ($4.7\ \sigma$)
Stars + GCs	301^{+5}_{-14}	$9.3^{+0.1}_{-0.2}$	206.0 ($20.1\ \sigma$)

NOTE.—The best-fit mass parameters (σ_0 and Υ_B) are given for the SIS and constant M/L models, given different sets of observational constraints. The difference in log likelihood between the two models is shown, along with the statistical significance at which the SIS model is preferred. The "Bayesian" probability for the SIS model is $(1 + e^{-\Delta \ln \mathscr{L}})^{-1} \simeq 1$, while that for the constant M/L model is $e^{-\Delta \ln \mathscr{L}}(1 + e^{-\Delta \ln \mathscr{L}})^{-1} \simeq e^{-\Delta \ln \mathscr{L}}$ for $\Delta \ln \mathscr{L} \gtrsim 2$.
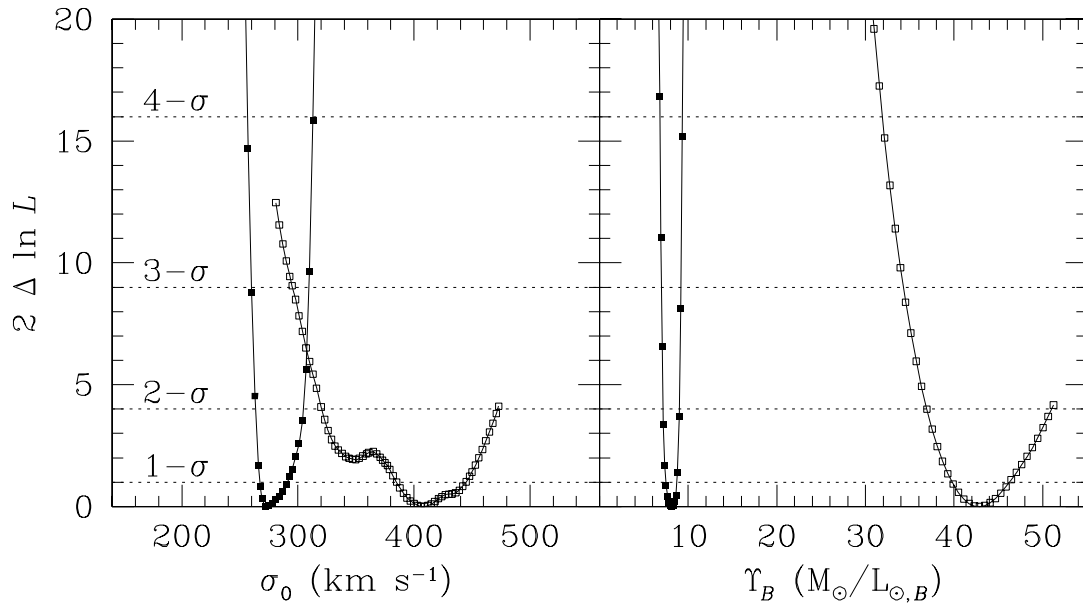
FIG. 4.—Log likelihood of the best-fit singular isothermal model (*left*) and constant mass-to-light ratio model (*right*) as a function of the mass parameters σ_0 and Υ_B. The filled squares show the fit to the stellar data and the open squares the fit to the GC data.

radii can the stellar kinematic data by itself further constrain the mass distribution.

We fit the GC data to the same two mass models (see Fig. 4 and Table 1). For the SIS model, we find $\sigma_0 = 409^{+36}_{-24}$ km s^{-1}; the fit of the best SIS solution to the data is shown in Figures 6–8. Note especially in Figure 7 that some of the higher order features of the observed LOSVDs are reproduced by the model. For the constant M/L model, we find $\Upsilon_B = 43 \pm 3$. This model fits the data much worse than

does the SIS model (5 σ significance). Here, the constant M/L model cannot reproduce the radially rising GC velocity dispersion (see Fig. 6). Also, $\Upsilon_B = 43$ is implausible for a standard stellar population, requiring an age $\geqslant 17$ Gyr and a metallicity [Fe/H] $\geqslant 0.50$ (Worthey 1994), so that even if mass traced light, the mass could not consist of a standard stellar population. Finally, note that $\Upsilon_B = 43 \pm 3$ is completely inconsistent with 8.1 ± 0.6 as obtained via the stellar
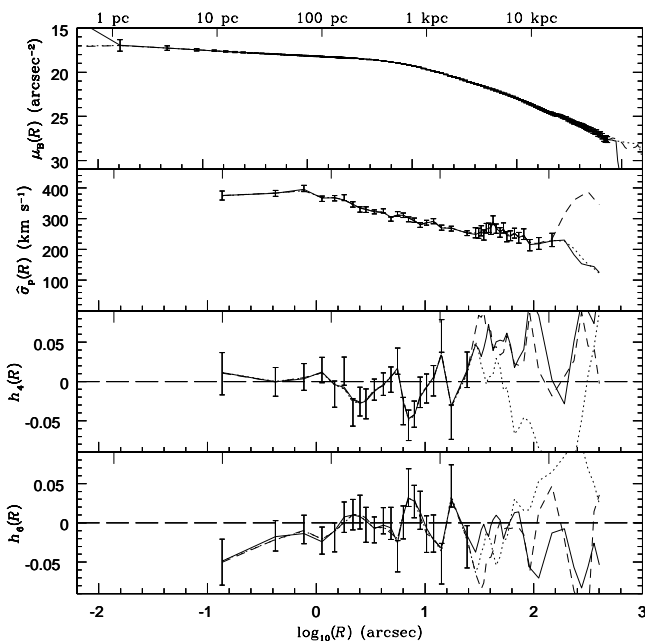

FIG. 5.—Fits to the M87 stellar data (*error bars*) for the best singular isothermal model ($\sigma_0 = 272$ km s^{-1}; *solid lines*), the best constant mass-to-light ratio model ($\Upsilon_B = 8.1$; *dotted lines*), and the best NFW2 model (see § 4.2; *dashed lines*). From top to bottom, the data are the radial profiles of the surface brightness, the velocity dispersion, and the fourth- and sixth-order Gauss-Hermite velocity moments. Note that $R_{\rm eff} \simeq 100''$.
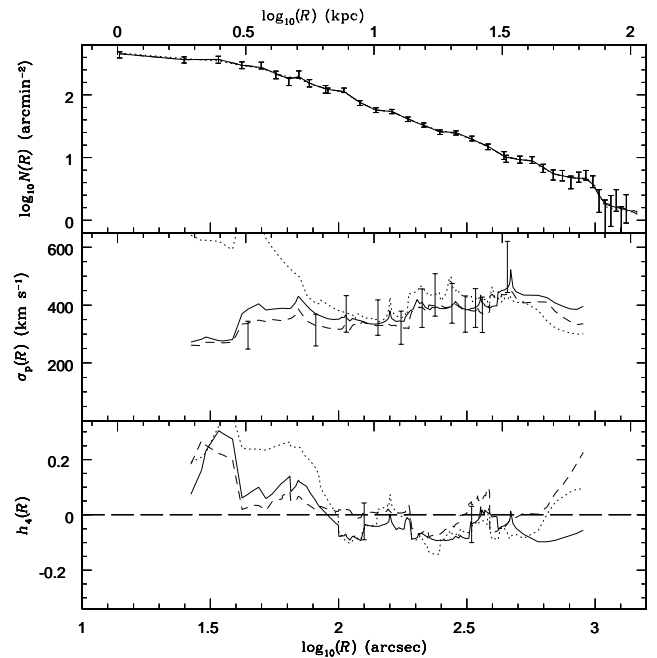

FIG. 6.—Fits to the M87 GC data (*error bars*) for the best singular isothermal model ($\sigma_0 = 409$ km s^{-1}; *solid lines*), the best constant mass-to-light ratio model ($\Upsilon_B = 42.9$; *dotted lines*), and the best NFW2 model (see § 4.2; *dashed lines*). From top to bottom, the data include the radial profiles of the surface density, the velocity dispersion, and the fourth-order Gauss-Hermite velocity moment. Note that only the surface density is actually fitted, while the other data are shown for comparative purposes only.
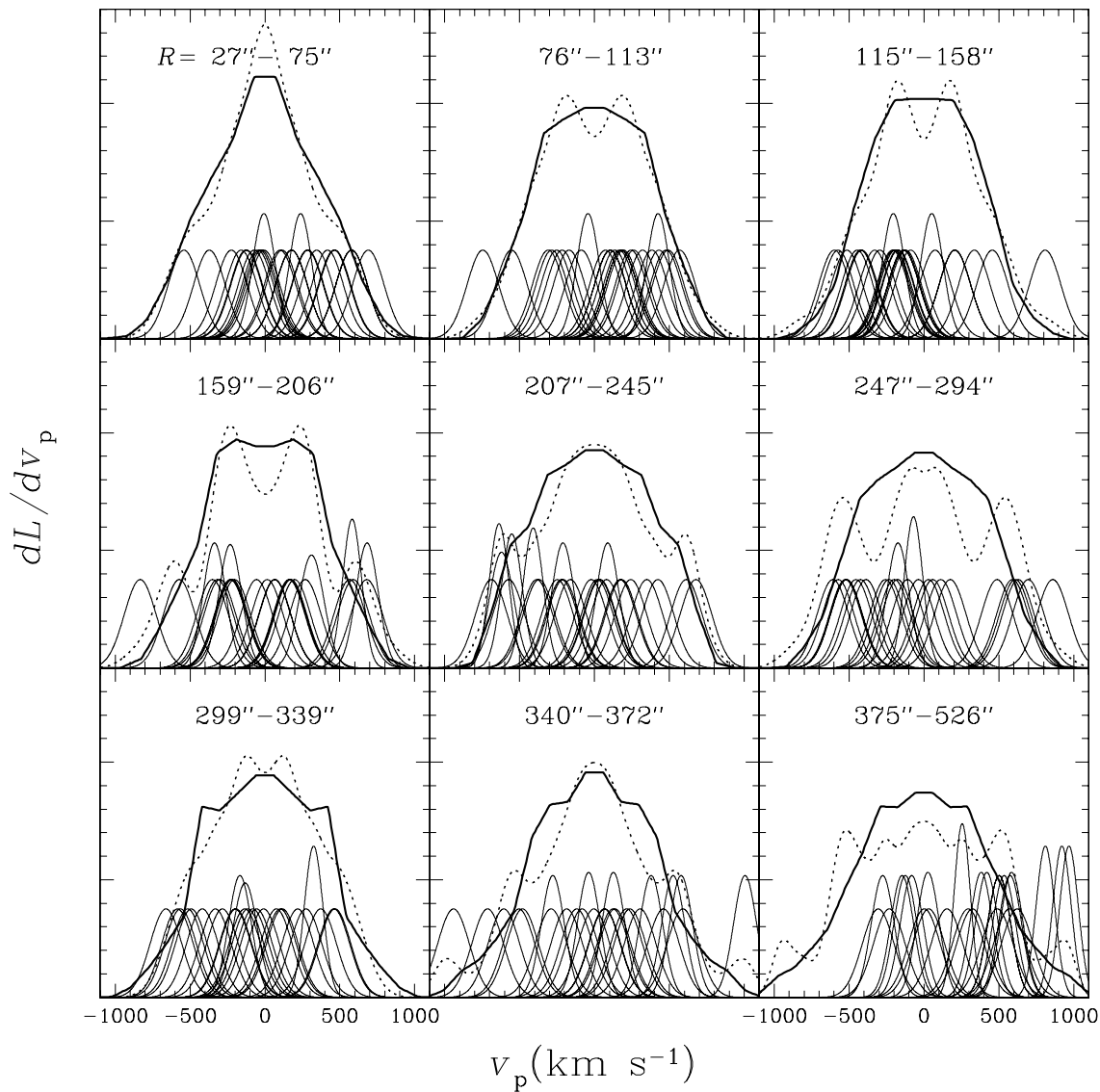
Fig. 7.—LOSVDs for the M87 GC system in nine radial bins. The heavy solid lines show the LOSVDs of the best-fit SIS model ($\sigma_0 = 409$ km s^{-1}) averaged in each bin. The light solid lines show the data (26 points in each bin). The dotted lines show simulated LOSVDs derived from the superposition of the data in each bin, symmetrized about $v_p = 0$. Compare with Fig. 3.

dynamics unless there is a drastic radial gradient in the stellar population. We thus conclude that the constant M/L model is definitively ruled out for M87, assuming standard gravitational dynamics. (Note that the 20 σ significance given in Table 1 is formal only and that, in practice, a number of systematic uncertainties will reduce this significance—but it can still be said that the result holds to a high significance level.)

4.2. Generalized Mass Models

With the constant M/L model ruled out, the next question is what the actual radial distribution of mass is in the system. The simple SIS model is seen to be inaccurate: the σ_0 mass parameters derived separately from the stellar and GC constraints are inconsistent at the 99% confidence level (see Fig. 4 and Table 1). That the GC-derived mass is *higher* than the stellar-derived mass implies that the radial mass profile $M(r)$ rises more steeply than isothermal ($\propto r$) in the outer parts. To make an initial estimation of $M(r)$, we use the spherical isotropic Jeans equations (see eq. [11] of

Sargent et al. 1978 and compare CR Fig. 6), modeling the stellar and GC subsystems separately. The stellar constraints imply $M \sim r^{0.9}$ out to $r \sim 150'' \sim 10$ kpc, while the GC constraints imply $M \sim r^{1.3}$ outside this radius (see Fig. 9). These crude Jeans models thus suggest that it would be fruitful to further explore two-component mass models consisting of a constant M/L galaxy plus a dark halo with $M(r)$ steeper than isothermal in the region of $r \sim 100''-500''$ (7–36 kpc).

We next use our orbit modeling methods to examine such a generalized mass model, where the form of the dark halo is based on the predictions from simulations of cosmologically motivated structure formation (e.g., Navarro, Frenk, & White 1996). This model has a total radial mass density profile of

$$\rho(r) = \Upsilon_B \, v_*(r) + \frac{\rho_0 \, r_s^3}{r(r + r_s)^2} \, ,$$

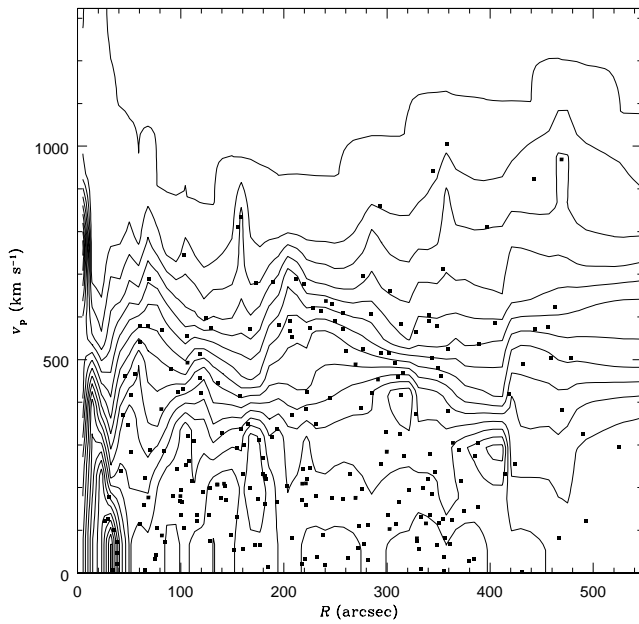where r_s is the break radius between the halo's inner r^{-1} profile and outer r^{-3} profile. We construct mass models

FIG. 8.—Contour plot of LOSVD ($I^{-1}dI/dv_p$) for the best-fit singular isothermal globular cluster system model ($\sigma_0 = 409$ km s^{-1}), normalized by the surface brightness at each radius R. The last contour represents zero intensity. The data are shown as squares. Note that the model LOSVD is peaked at small radii ($R < 50''$) and is flat and even double-peaked elsewhere.

with a variety of the parameters (Υ_B, ρ_0, r_s), fitting the combined stellar and GC constraints, and report the results of our three best models in Table 2 (see also Figs. 5 and 6). Note that each distinct model begins with a set of kernels calculated for two fixed parameters ($\Upsilon_B/\rho_0, r_s$) and may then have its overall mass normalization scaled linearly to best fit the data.

All these models (NFW1, NFW2, and NFW3) can produce better fits to the full data set than can the best SIS model (at the 98% significance level) and thus probably better approximate the overall mass distribution. The mass profiles of these models are consistent with $M(r)$ derived from the galaxy's X-ray halo (Nulsen & Böhringer 1995), both in mass normalization and in density exponent (see Fig. 9). Both our NFW models and the X-ray model have density profiles that decline more gradually than isothermal in the galaxy's outer parts (e.g., $\rho \sim r^{-1.5}$ at $r \sim 200'' \sim 15$ kpc), giving a circular velocity curve $v_c(r)$ that continues rising at large radii (Fig. 10). Most elliptical galaxies have a
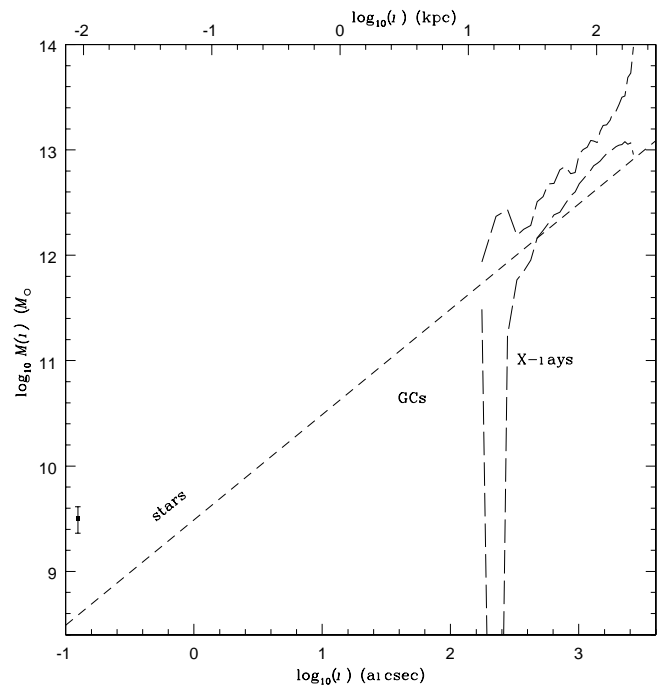

FIG. 9.—Radial mass profile of M87. The heavy solid lines show estimates from the Jeans equations using the stars and GCs separately. The long-dashed lines show confidence limits from the X-ray analysis of Nulsen & Böhringer (1995). The other lines show the best orbit models fitted to the combined star and GC data for the constant M/L model (*dotted line*), the SIS model (*dashed line*), and the NFW2 model (*light solid line*). The point with error bars shows the estimated mass of the central supermassive black hole (Macchetto et al. 1997).

constant or declining $v_c(r)$ at these radii (Gerhard et al. 2001; the notable exception is the Fornax cD galaxy NGC 1399) so this is strong evidence that the dark matter at large radii is associated with the Virgo Cluster itself.

A caveat about these new models is that the mass normalization from the stellar and GC data separately is again inconsistent (at the 1–2 σ level). This may indicate that a still more accurate mass model $M(r)$ could be found to fit all the existing constraints (possibly one with a larger, less concentrated cluster halo as in McLaughlin 1999) and/or that one or both of the dynamic subsystems (stars and GCs) would be better modeled without the assumption of spherical symmetry. Further exploration of more detailed models would be useful but outside the scope of this project.

TABLE 2

COMBINED M87 MODEL SOLUTIONS

| | MODEL PARAMETERS | | | | |
MODEL NAME	Υ_B ($M_\odot/L_{\odot, B}$)	σ_0 (km s^{-1})	$\rho_0 r_s^3$ ($\times 10^{12} M_\odot$)	r_s(arcsec; kpc)	$\Delta \ln \mathscr{L}$
Constant M/L......	9.3	...	...	...	208.3 (20.3 σ)
SIS..................	...	301	...	...	3.7 (2.3 σ)
NFW1	5.6	...	0.9	500; 36	0.4 (0.8 σ)
NFW2	5.9	...	2.4	939.3; 68	...
NFW3	6.5	...	4.8	1800; 131	0.6 (0.9 σ)

NOTE.—The best-fit model parameters are given for each model (see text for description), given combined stellar and GC constraints. The difference in log likelihood between each model and the best overall model (NFW2) is shown along with the statistical significance at which the model is "dispreferred."
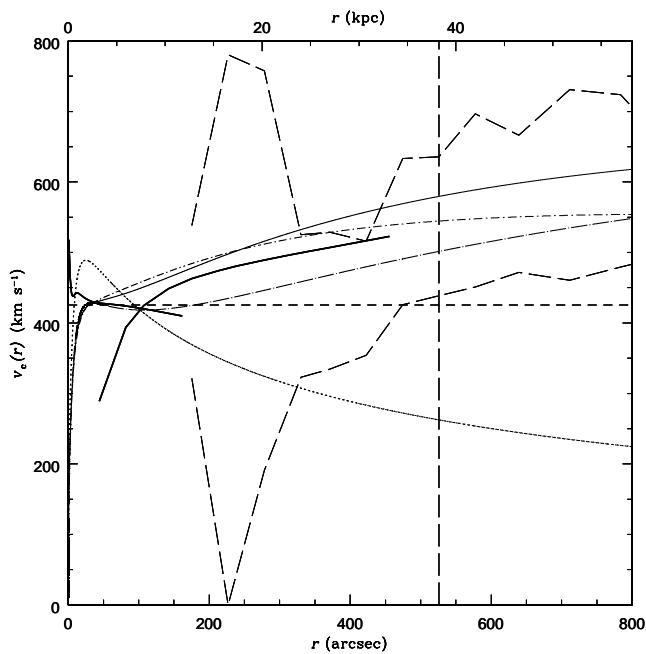
FIG. 10.—Circular velocity profile of M87 for different models. Line styles are as in Fig. 9, with the addition of the NFW1 (*short-dash–dotted line*) and NFW3 (*long-dash–dotted line*) models. The vertical dashed line indicates the outer radius of the region constrained by the GC data.

FIG. 12.—Velocity anisotropy of GC system as a function of radius for different mass models (see Fig. 11 for line descriptions). The vertical dashed lines indicate the radial region constrained by the GC velocity data.

4.3. Orbit Anisotropies

We have not implemented any method of rigorously exploring the range of DF functional forms permitted by the data, so the following results are meant to be suggestive rather than conclusive. Figure 11 illustrates the stellar orbital characteristics of the overall best-fit solutions, where
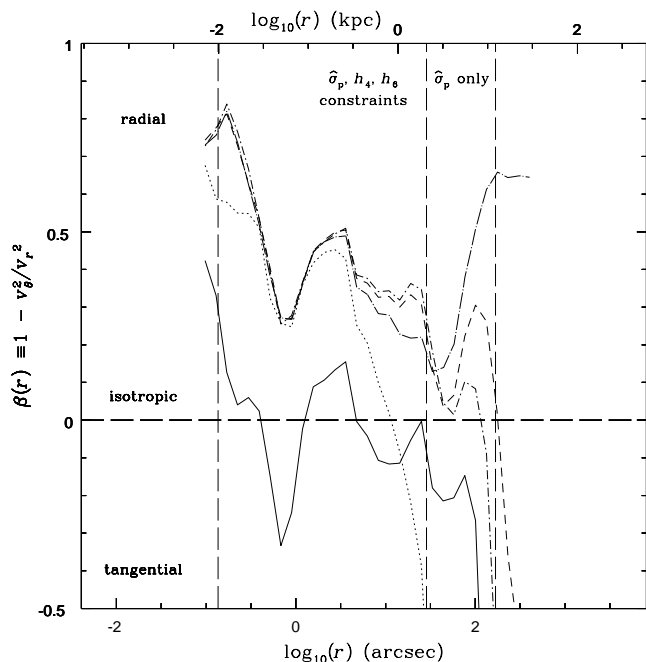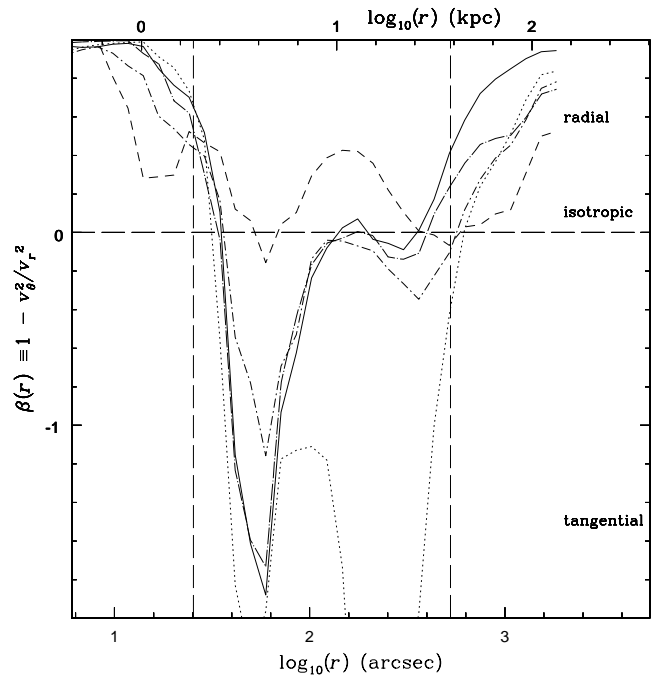

FIG. 11.—Stellar orbital anisotropy as a function of radius for the overall best-fit solutions from five different mass models: constant M/L (*dotted line*), SIS (*solid line*), NFW1 (*short-dash–dotted line*), NFW2 (*dashed line*), and NFW3 (*long-dash–dotted line*). The vertical dashed lines indicate the radial regions constrained by the stellar kinematic data.

the mean anisotropy is characterized by the parameter $\beta \equiv 1 - \langle v_\theta^2 \rangle / \langle v_r^2 \rangle$. The NFW solutions have a somewhat radial DF in the region constrained by the kinematic data ($r \sim 0\farcs15$–$170'' \sim 0.01$–12 kpc). The downward dive in β near $r = 0\farcs7$ is due to the sharp turnover in $\hat{\sigma}_p(R)$ inside that radius. Real galaxies presumably have smooth $\beta(r)$ profiles, but with no smoothness imposed, our models are somewhat noisy because of the ill-conditioning of this inversion problem. Also, the region $r \lesssim 1''$ is within the radius of influence of the central supermassive black hole (with mass $M_{\rm BH} = 3.2 \pm 0.9 \times 10^9 \ M_\odot$; Macchetto et al. 1997) and thus has not been accurately treated by our models. In summary, our best models indicate mild radial orbit anisotropy ($\beta = 0.2$–0.5) for the well-constrained stellar region of the galaxy ($r \sim 1''$–$30'' \sim 0.1$–2 kpc)—a characteristic that has turned out to be quite typical for bright elliptical galaxies (see Gerhard et al. 2001 and references therein).

Figure 12 shows the orbital characteristics of the globular cluster system for the overall best-fit solutions. There is considerable variation between the best NFW solutions, so we cannot yet strongly constrain the GC anisotropy, except to note that it seems roughly isotropic at large radii ($r \sim 100''$–$500'' \sim 10$–40 kpc). This seems to contradict the tangential anisotropy one would expect given the flat and double-peaked LOSVDs seen in the data and in the models that fit only the GC data (see § 2.4 and Figs. 7 and 8)—illustrating further the need for a mass model that better fits both the stellar and GC constraints. Note that the solutions' radial anisotropy at $r \lesssim 40'' \lesssim 3$ kpc should not be considered highly significant since there are only eight GC velocities measured inside that projected radius.

5. CONCLUSIONS

We have developed a very general spherical orbit modeling method that makes full use of all the information in a set of discrete velocity data and have applied it to the giant

elliptical galaxy M87 using all the available dynamic constraints (measurements of the spatial distribution and the kinematics of the stars and of the globular clusters). By comparing two simple mass models—a constant mass-to-light ratio galaxy and a singular isothermal sphere—we find that a constant M/L is ruled out to a high level of significance.

We further implement some more generalized mass models in order to more accurately represent the galaxy as consisting of a constant M/L stellar system plus a dark halo. We find improved solutions that have a dark halo density profile decreasing more slowly than $\sim r^{-2}$ at large radii (10–40 kpc). This very extended halo seems best interpreted as belonging to the Virgo Cluster itself rather than to M87.

There is substantial room for improvement in our M87 models. First, measurements of higher order velocity moments for the stars are available to only $\sim 0.3 R_{\mathrm{eff}}$. Such measurements at larger radii would be quite helpful in better constraining the models and can be most efficiently obtained by measuring discrete velocities of the galaxy's planetary nebulae. Second, a larger range of mass models could be explored to find solutions that fit the stellar and GC data together more consistently, and third, future models could relax our assumption of spherical symmetry, providing a more accurate model of the system in its outer parts, where flattening is seen in both the stellar and GC systems.

The same techniques should also be applied to other, non-cD giant elliptical galaxies in clusters (such as NGC 4472) as well as to galaxies in the field. The different formational histories of these galaxies (via mergers, accretion, etc.) may result in significantly different mass distributions and dynamics. Furthermore, the colors, abundances, and spatial distributions of the GCs in M87 and other galaxies indicate that they comprise two or more distinct populations (see, e.g., Neilsen & Tsvetanov 1999; Gebhardt & Kissler-Patig 1999). It would be interesting to use our orbit modeling methods to look for any dynamic differences between these populations, which may shed light on their formation histories, for which several different scenarios have been proposed (see, e.g., Ashman & Zepf 1992; Forbes, Brodie, & Grillmair 1997; Harris, Harris, & McLaughlin 1998; Côté, Marzke, & West 1998). The available set of kinematic tracers observed in the outer parts of early-type galaxies is now increasing rapidly, and we are hopeful that a much clearer picture of galaxy halos is forthcoming.

REFERENCES

Arnaboldi, M., Freeman, K. C., Gerhard, O., Matthias, M., Kudritzki, R. P., Méndez, R. H., Capaccioli, M., & Ford, H. 1998, ApJ, 507, 759
Ashman, K. M., & Zepf, S. E. 1992, ApJ, 384, 50
Binney, J., & Mamon, G. A. 1982, MNRAS, 200, 361
Binney, J., & Tremaine, S. 1987, Galactic Dynamics (Princeton: Princeton Univ. Press)
Boroson, T. A., Thompson, I. B., & Shectman, S. A. 1983, AJ, 88, 1707
Burstein, D., Davies, R. L., Dressler, A., Faber, S. M., Stone, R. P. S., Lynden-Bell, D., Terlevich, R. J., & Wegner, G. 1987, ApJS, 64, 601
Caon, N., Capaccioli, M., & Rampazzo, R. 1990, A&AS, 86, 429
Carollo, C. M., de Zeeuw, P. T., van der Marel, R. P., Danziger, I. J., & Qian, E. E. 1995, ApJ, 441, L25
Carter, D., & Dixon, K. L. 1978, AJ, 83, 574
Ciardullo, R., Jacoby, G. H., & Dejonghe, H. B. 1993, ApJ, 414, 454
Cohen, J. 1986, AJ, 92, 1039
———. 2000, AJ, 119, 162
Cohen, J. G., & Ryzhov, A. 1997, ApJ, 486, 230 (CR)
Côté, P., Marzke, R. O., & West, M. J. 1998, ApJ, 501, 554
Cretton, N., Rix, H.-W., & de Zeeuw, P. T. 2000, ApJ, 536, 319
Cretton, N., & van den Bosch, F. C. 1999, ApJ, 514, 704
Davies, R. L., & Birkinshaw, M. 1988, ApJS, 68, 409
de Vaucouleurs, G., de Vaucouleurs, A., Corwin, H. G., Jr., Buta, R. J., Paturel, H. G., & Fouqué, P. 1991, Third Reference Catalogue of Bright Galaxies (New York: Springer)
de Vaucouleurs, G., & Nieto, J.-L. 1978, ApJ, 220, 449
Dressler, A., & Richstone, D. O. 1990, ApJ, 348, 120
Duncan, M. J., & Wheeler, J. C. 1980, ApJ, 237, L27
Emsellem, E., Dejonghe, H., & Bacon, R. 1999, MNRAS, 303, 495
Fabbiano, G. 1989, ARA&A, 27, 87
Federici, L., Bònoli, F., Ciotti, L., Fusi Pecci, F., Marano, B., Lipovetsky, V. A., Neizvestny, S. I., & Spassova, N. 1993, A&A, 274, 87
Forbes, D. A., Brodie, J. P., & Grillmair, C. J. 1997, AJ, 113, 1652
Gebhardt, F., & Fischer, P. 1995, AJ, 109, 209
Gebhardt, K., & Kissler-Patig, M. 1999, AJ, 118, 1526
Gebhardt, K., et al. 2000, AJ, 119, 1157
Gerhard, O., Jeske, G., Saglia, R. P., & Bender, R. 1998, MNRAS, 295, 197
Gerhard, O., Kronawitter, A., Saglia, R. P., & Bender, R. 2001, AJ, 121, 1936
Grillmair, C. J., Freeman, K. C., Bicknell, G. V., Carter, D., Couch, W. J., Sommer-Larsen, J., & Taylor, K. 1994, ApJ, 422, L9
Haller, J. W., & Melia, F. 1996, ApJ, 464, 774
Harris, W. E. 1986, AJ, 91, 822
Harris, W. E., Harris, G. L. H., & McLaughlin, D. E. 1998, AJ, 115, 1801
Heisler, J., Tremaine, S., & Bahcall, J. N. 1985, ApJ, 298, 8
Hernquist, L. 1990, ApJ, 356, 359
Huchra, J., & Brodie, J. 1987, AJ, 93, 779

Hui, X., Ford, H. C., Freeman, K. C., & Dopita, M. A. 1995, ApJ, 449, 592
Jarvis, B. J., & Peletier, R. F. 1991, A&A, 247, 315
Kent, S. M. 1990, MNRAS, 247, 702
Kissler-Patig, M., & Gebhardt, K. 1998, AJ, 116, 2237
Kissler-Patig, M., Grillmair, C. J., Meylan, G., Brodie, J. P., Minniti, D., & Goudfrooij, P. 1999, AJ, 117, 1206
Kronawitter, A., Saglia, R. P., Gerhard, O., & Bender, R. 2000, A&AS, 144, 53
Kundu, A., Whitmore, B. C., Sparks, W. B., Macchetto, F. D., Zepf, S. E., & Ashman, K. M. 1999, ApJ, 513, 733
Lauer, T. R., et al. 1992, AJ, 103, 703
Macchetto, F., Marconi, A., Axon, D. J., Capetti, A., Sparks, W., & Crane, P. 1997, ApJ, 489, 579
Mathieu, A., & Dejonghe, H. 1999, MNRAS, 303, 455
McLaughlin, D. E. 1999, ApJ, 512, L9
McLaughlin, D. E., Harris, W. E., & Hanes, D. A. 1993, ApJ, 409, L45
———. 1994, ApJ, 422, 486
Merritt, D. 1993, ApJ, 413, 79
Merritt, D., Meylan, G., & Mayor, M. 1997, AJ, 114, 1074
Merritt, D., & Oh, S. P. 1997, AJ, 113, 1279
Merritt, D., & Saha, P. 1993, ApJ, 409, 75
Merritt, D., & Tremblay, B. 1993, AJ, 106, 2229
Mould, J. R., Oke, J. B., de Zeeuw, P. T., & Nemec, J. M. 1990, AJ, 99, 1823
Mould, J. R., Oke, J. B., & Nemec, J. M. 1987, AJ, 93, 53
Navarro, J. F., Frenk, C. S., & White, S. D. M. 1996, ApJ, 462, 563
Neilsen, E. H., Jr., & Tsvetanov, Z. I. 1999, ApJ, 515, L13
Newton, A. J., & Binney, J. 1984, MNRAS, 210, 711
Nulsen, P. E. J., & Böhringer, H. 1995, MNRAS, 274, 1093
Pierce, M. J., Welch, D. L., McClure, R. D., van den Bergh, S., Racine, R., & Stetson, P. B. 1994, Nature, 371, 385
Press, W. H., Teukolsky, S. A., Vetterling, W. T., & Flannery, B. P. 1992, Numerical Recipes in C (2d ed.; Cambridge: Cambridge Univ. Press)
Richstone, D. O., & Tremaine, S. 1984, ApJ, 286, 27
———. 1985, ApJ, 296, 370
Rix, H.-W., de Zeeuw, P. T., Cretton, N., van der Marel, R. P., & Carollo, C. M. 1997, ApJ, 488, 702
Romanowsky, A. J., & Kochanek, C. S. 1999, ApJ, 516, 18 (Paper I)
Saglia, R. P., Kronawitter, A., Gerhard, O., & Bender, R. 2000, AJ, 119, 153
Sargent, W. L. W., Young, P. J., Boksenberg, A., Shortridge, K., Lynds, C. R., & Hartwick, F. D. A. 1978, ApJ, 221, 731
Schombert, J. M. 1986, ApJS, 60, 603
Schwarzschild, M. 1979, ApJ, 232, 236
Sembach, K. R., & Tonry, J. L. 1996, AJ, 112, 797 (ST)
Strom, S. E., Forte, J. C., Harris, W. E., Strom, K. M., Wells, D. C., & Smith, M. G. 1981, ApJ, 245, 416
Tenjes, P., Einasto, J., & Haud, U. 1991, A&A, 248, 395

Tonry, J. L. 1983, ApJ, 266, 58

Tremblay, B., Merritt, D., & Williams, T. B. 1995, ApJ, 443, L5

van der Marel, R. P. 1994, MNRAS, 270, 271 (vdM)

van der Marel, R. P., Cretton, N., de Zeeuw, P. T., & Rix, H.-W. 1998, ApJ, 493, 613

van der Marel, R. P., Evans, N. W., Rix, H.-W., White, S. D. M., & de Zeeuw, T. 1994, MNRAS, 271, 99

van der Marel, R. P., & Franx, M. 1993, ApJ, 407, 525

Winsall, M. L., & Freeman, K. C. 1993, A&A, 268, 443

Worthey, G. 1994, ApJS, 95, 107

Zeilinger, W. W., Møller, P., & Stiavelli, M. 1993, MNRAS, 261, 175

Zepf, S. E., Beasley, M. A., Bridges, T. J., Hanes, D. A., Sharples, R. M., Ashman, K. M., & Geisler, D. 2000, AJ, 120, 2928